JACS
JOURNAL OF THE AMERICAN CHEMICAL SOCIETY
pubs.acs.org/JACS
Article

Atomically Dispersed Zn/Co−N−C as ORR Electrocatalysts for Alkaline Fuel Cells

Weixuan Xu,[‖] Rui Zeng,[‖] Michael Rebarchik,[‖] Alvaro Posada-Borbón, Huiqi Li, Christopher J. Pollock, Manos Mavrikakis,* and Héctor D. Abruña*

Cite This: https://doi.org/10.1021/jacs.3c11355
Read Online

ABSTRACT: Hydrogen fuel cells have drawn increasing attention as one of the most promising next-generation power sources for future automotive transportation. Developing efficient, durable, and low-cost electrocatalysts, to accelerate the sluggish oxygen reduction reaction (ORR) kinetics, is urgently needed to advance fuel cell technologies. Herein, we report on metal−organic frameworks-derived nonprecious dual metal single-atom catalysts (SACs) (Zn/Co−N−C), consisting of Co−N_4 and Zn−N_4 local structures. These catalysts exhibited superior ORR activity with a half-wave potential ($E_{1/2}$) of 0.938 V versus RHE (reversible hydrogen electrode) and robust stability ($\Delta E_{1/2}$ = −8.5 mV) after 50k electrochemical cycles. Moreover, this remarkable performance was validated under realistic fuel cell working conditions, achieving a record-high peak power density of ∼1 W cm^{-2} among the reported SACs for alkaline fuel cells. *Operando* X-ray absorption spectroscopy was conducted to identify the active sites and reveal catalytic mechanistic insights. The results indicated that the Co atom in the Co−N_4 structure was the main catalytically active center, where one axial oxygenated species binds to form an O_{ads}−Co−N_4 moiety during the ORR. In addition, theoretical studies, based on a potential-dependent microkinetic model and core-level shift calculations, showed good agreement with the experimental results and provided insights into the bonding of oxygen species on Co−N_4 centers during the ORR. This work provides a comprehensive mechanistic understanding of the active sites in the Zn/Co−N−C catalysts and will pave the way for the future design and advancement of high-performance single-site electrocatalysts for fuel cells and other energy applications.

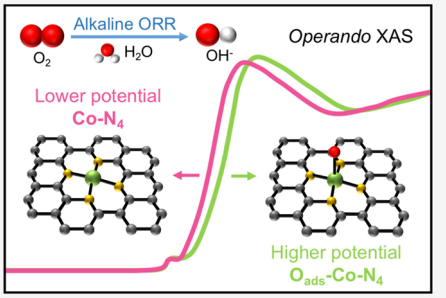

INTRODUCTION

Hydrogen fuel cells have been recognized as one of the most promising high-efficiency regenerative energy-conversion devices for electric vehicles, portable electronic devices, and stationary applications.[1−3] However, in order to accelerate the sluggish kinetics of the oxygen reduction reaction (ORR) at the cathode, significant amounts of expensive Pt-based metal catalysts are required in proton exchange membrane fuel cells (PEMFCs), operating at low pH, for high power density applications (>1 W cm^{-2}).[4,5] The high catalyst cost, up to 40% of the total cost, has hindered the large-scale application and deployment of PEMFCs.[6] Anion exchange membrane fuel cells (AEMFCs) have emerged as an alternative because they enable the use of nonprecious metal electrocatalysts, which exhibit improved stability in alkaline media compared to acidic electrolytes.[7,8] To facilitate the ORR in alkaline media, tremendous efforts have been expended to investigate and develop various cost-effective nonprecious metal catalysts, including perovskites,[9−11] transition metal oxides,[12−14] transition metal nitrides,[15−17] and metal-containing nitrogen-doped carbons (M−N−C).[18−20]

Recently, single-atom catalysts (SACs), ultimately downsizing the metal active centers to isolated single metal atoms, have attracted increased attention for electrocatalysis.[21−23] With atomic metal dispersity, SACs offer distinct advantages such as maximized atom-utilization efficiency, well-defined active centers, and remarkable intrinsic activity.[24,25] Importantly, the well-defined single-atom site can serve as an ideal model to provide atomic-level insights into active centers and thus foster an in-depth understanding of catalytic reaction mechanisms. Typically, single-metal atoms need to be anchored on a supporting substrate through a strong interaction to stabilize these single atoms with high surface free energies and avoid metal aggregation.[26,27] Metal−organic frameworks (MOFs), a class of porous materials assembled by metal nodes and versatile organic linkers, have emerged as one of the most promising scaffolds and precursors for porous carbon-supported SACs. The spatial separation of metal nodes in the periodic structures of MOFs prevents metal agglomeration during pyrolysis, enabling the formation of single-atom sites.[28,29] The high surface areas and porous structures of

Received: October 12, 2023
Revised: January 2, 2024
Accepted: January 3, 2024

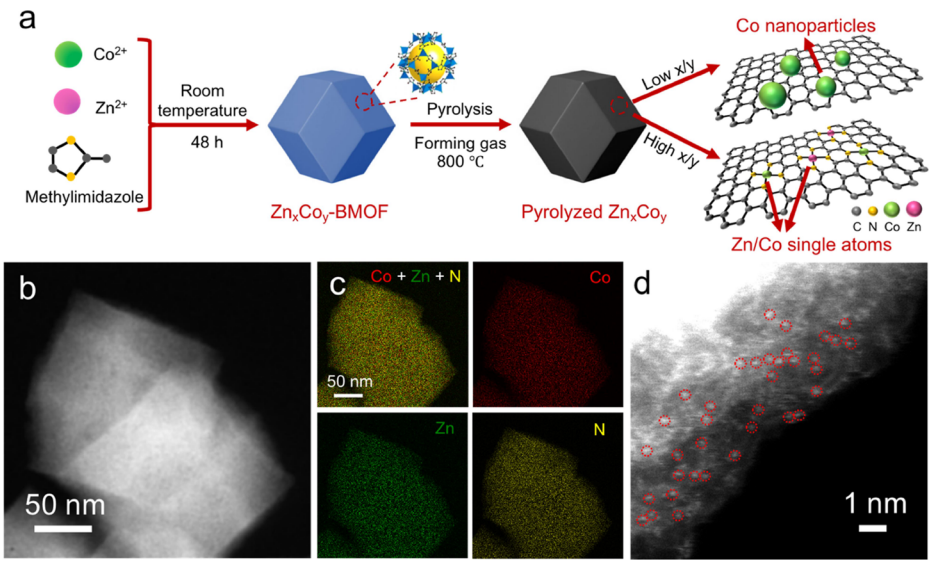

Figure 1. Synthesis and structural characterization of BMOF-derived Zn_xCo_y materials. (a) Schematic synthesis procedure of BMOF-derived Zn_xCo_y. (b) HAADF-STEM image of pyrolyzed $Zn_{20}Co$. (c) EELS elemental mapping of Co (red), Zn(green), N(yellow), and their composite mapping of Co+Zn+N. (d) Magnified atomic-scale HAADF-STEM image of pyrolyzed $Zn_{20}Co$. The bright spots, corresponding to Co or Zn atoms, are marked by red circles.

MOF-derived substrates facilitate mass transport and expose more active sites for the catalytic process.[30−32] Moreover, the nitrogen species from N-containing organic linkers (such as imidazole groups) can bind to metal centers to form single-atom M−N−C structures, which are believed to be responsible for the accelerated kinetics of the ORR.[33−35] The rational design of bimetallic MOFs holds great promise for developing dual-site single-atom materials, such as atomically dispersed Zn/Co or Zn/Cu in N-doped carbon.[36−38] The incorporation of Zn centers in the precursors emerges as a promising strategy for synthesizing M−N−C structures because the evaporation of Zn centers at high-temperature pyrolysis facilitates the formation of hierarchical pore structures and the generation of sparsely distributed single-atom metal sites. In addition, Zn−N−C can serve as a template for the synthesis of other M−N−C materials. For instance, Fellinger's group utilized $Zn-N_4$ sites in Zn−N−C as an active site imprint to prepare atomically dispersed Fe−N−C with a high Fe loading (3.12 wt %) via a transmetalation reaction.[39,40]

Despite the significant progress made in designing and developing SACs for ORR, insights into the evolution of catalytic sites and underlying catalytic mechanisms are still rare due to the challenges of directly probing atomic-level active sites. High sensitivity and sufficient spatiotemporal resolution are critical for characterizing SACs under catalytic conditions to gain a fundamental understanding of their behavior. Over the past few decades, intense efforts have been made to develop *in situ*/*operando* techniques that enable tracking the dynamic evolution of single atoms in real time, such as *in situ* transmission electron microscopy (TEM),[41,42] *in situ* Fourier-transform infrared spectroscopy (FTIR),[43] *in situ*/*operando* X-ray absorption spectroscopy (XAS), and others.[44−46] Among these techniques, *in situ*/*operando* XAS represents one of the most powerful methods for capturing dynamic changes of single-atom sites, providing real-time information on both electronic structure and local geometry via X-ray absorption near-edge structure (XANES) and extended X-ray absorption fine structure (EXAFS), respectively. For example, Zitolo et al.[47] performed *operando* XAS to study the electronic state evolution of $Co-N-C(Co_{0.5})$ and $Fe-N-C(Fe_{0.5})$ under ORR conditions. They found that a Fe−O bond formed in both the O_2-saturated and N_2-saturated electrolytes, while Co sites were less oxophilic so that a Co−O bond was formed only in the O_2-saturated electrolytes. Via *operando* XAS, Du and co-workers[48] revealed that a geometric structural distortion of CuN_2C_2 single-atom sites was induced by O-containing species under ORR conditions. An optimized distortion can facilitate electron transfer from Cu to adsorbed O, thus enhancing the ORR activity.

In this work, we report on a group of bimetallic MOF (BMOF)-derived Zn_xCo_y (x/y = 1, 5, 10, 15, 20, 25) materials. Among them, BMOF-derived $Zn_{20}Co$ features atomically dispersed Co and Zn sites coordinated with N atoms, forming $Zn-N_4$ and $Co-N_4$ local structural configurations (denoted as Zn/Co−N−C). The structure and composition of the electrocatalysts were comprehensively characterized via a range of techniques, including X-ray diffraction (XRD), inductively coupled plasma optical emission spectroscopy (ICP-OES), scanning transmission electron microscopy (STEM) imaging, electron energy loss spectroscopy (EELS) elemental mapping, X-ray photoelectron spectroscopy (XPS), and XAS. Through electrochemical measurements in alkaline electrolytes, we demonstrated that BMOF-derived $Zn_{20}Co$ displayed superior activity and long-term stability toward the ORR. In H_2-O_2 fuel cell testing, using a BMOF-derived $Zn_{20}Co$ as a cathode catalyst, we were able to achieve a high peak power density (PPD) of ∼1 W cm^{-2} at an ultralow Co loading of 8 μg_{Co} cm^{-2}, representing one of the highest performances among reported single-atom cathode catalysts in AEMFCs.[45,49−51] To further unveil the nature of the catalytic sites in the Zn/Co−N−C materials, *operando* XAS was performed to track the dynamic electronic and structural changes under the ORR conditions. The real-time observations suggested that $Co-N_4$ structures served as the main active centers for the ORR, where an oxygenated species can be adsorbed on the Co center in an axial direction during the

https://doi.org/10.1021/jacs.3c11355
J. Am. Chem. Soc. XXXX, XXX, XXX−XXX

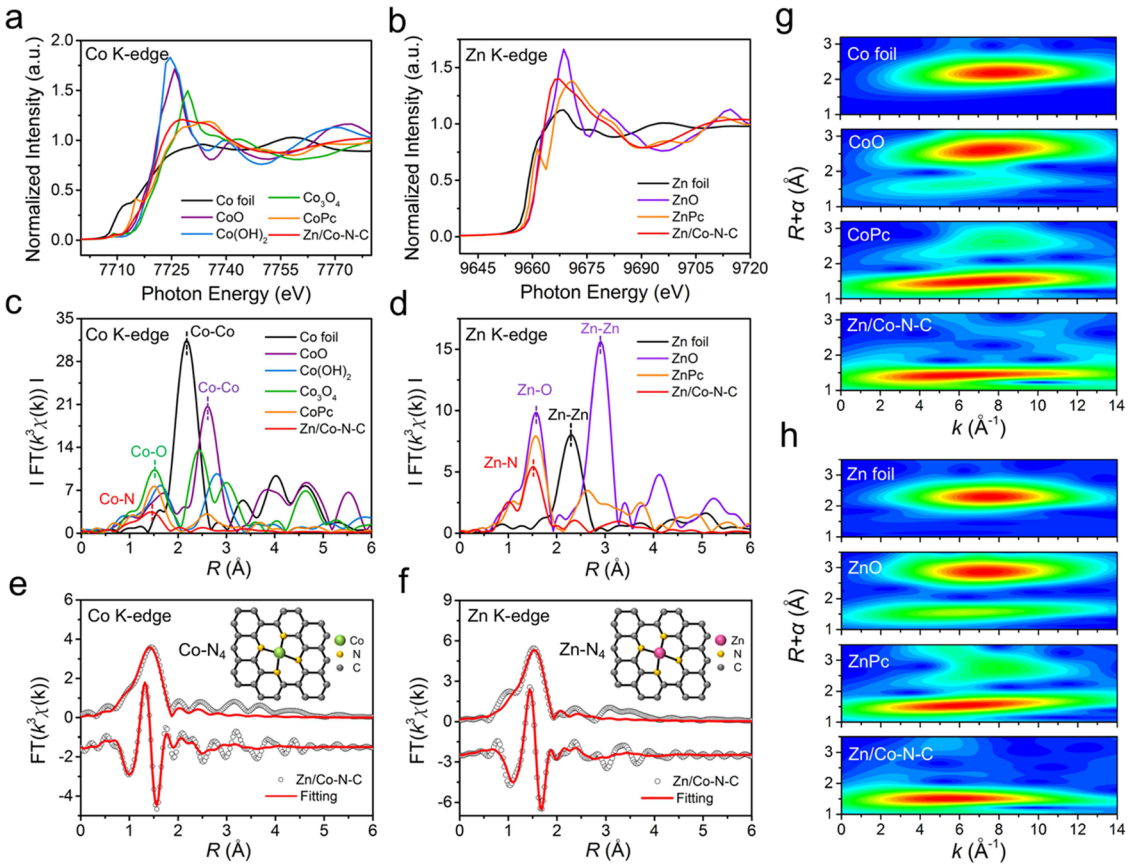

Figure 2. Spectroscopic characterization of Zn_{20}Co-BMOF-derived Zn/Co−N−C. (a) Normalized Co K-edge XANES and (c) k^3-weighted FT-EXAFS spectra (without phase correction) of Zn_{20}Co-BMOF-derived Zn/Co−N−C and Co references: Co foil, CoO, $Co(OH)_2$, Co_3O_4 and cobalt phthalocynine (CoPc). (b) Normalized Zn K-edge XANES and (d) k^3-weighted FT-EXAFS spectra of Zn_{20}Co-BMOF-derived Zn/Co−N−C and Zn references: Zn foil, ZnO and zinc phthalocynine (ZnPc). (e) Corresponding Co K-edge k^3-weighted FT-EXAFS fitting curves of Zn_{20}Co-BMOF-derived Zn/Co−N−C at R space (R magnitude and R imaginary). (f) Corresponding Zn K-edge k^3-weighted FT-EXAFS fitting curves of Zn_{20}Co-BMOF-derived Zn/Co−N−C at R space (R magnitude and R imaginary). (g) Co K-edge WT-EXAFS contour plots of Co foil, CoO, CoPc, and Zn/Co−N−C. (h) Zn K-edge WT-EXAFS contour plots of Zn foil, ZnO, ZnPc, and Zn/Co−N−C.

ORR process. To further investigate the metal centers of the Co−N_4 and Zn−N_4 sites under reaction conditions, a potential-dependent microkinetic model (MKM) was developed using density functional theory (DFT)-derived energetics. The model showed good agreement with the experimental results, which indicated that Co−N_4 was the active site for the ORR. It also provided insights into the adsorption of oxygen species on the Co−N_4 centers at elevated potentials. Core-level shift (CLS) calculations revealed distinct shifts of the 1s core−electron of the Co centers for each ORR reaction intermediate. Adsorption of oxygen-related species on the Co−N_4 centers led to a shift toward higher binding energy (BE), consistent with the positive edge shifts observed in *operando* XANES. The combined experimental and theoretical investigation in this work provides a fundamental understanding of the underlying catalytic mechanism of single-atom electrocatalysts toward the ORR and offers valuable insights into the design and development of high-performance electrocatalysts for fuel cells.

RESULTS AND DISCUSSION

Synthesis and Structural Characterization. BMOF-derived Zn_xCo_y materials with different ratios of Zn to Co (x/y) were prepared via a facile method, as indicated in Figure 1a (details in the Experimental Section). By variation of the x/y ratio, BMOF-Zn_xCo_y precursors can form Co metal nanoparticles or dispersed Zn/Co atoms supported on nitrogen-doped carbon materials after high-temperature pyrolysis. The powder XRD patterns of the as-synthesized Zn_xCo_y-BMOFs are shown in Figure S1a, which are consistent with the simulated ZIF-67 and ZIF-8 references. After high-temperature pyrolysis at 800 °C, most Zn centers in BMOFs evaporate away, and the resulting metal loadings are summarized in Table S1 based on ICP results. The Co loading decreased from 15.28 to 1.38 wt % when the ratio of Zn/Co (x/y) increased from 1/1 to 25/1. The XRD patterns of pyrolyzed Zn_xCo_y are presented in Figure S1b. For samples with relatively high Co content, such as ZnCo, Zn_5Co and Zn_{10}Co, the diffraction peaks near 45°, 52°, and 76° were ascribed to (111), (200), and (220) planes, respectively, from face-centered cubic (fcc) metallic Co (ICSD#44989). For low-Co-content samples such as Zn_{15}Co, Zn_{20}Co, and Zn_{25}Co, no sharp characteristic diffraction peaks were observed, ruling out the formation of large metal particles/clusters. Here, the increasing fraction of Zn in the MOF precursors plays a significant role in "diluting" the Co nodes and expanding the adjacent distances of Co centers, which avoid the aggregation of Co atoms in the heat treatment and help form atomically dispersed metal sites.

The morphologies of pyrolyzed Zn_xCo_y were characterized via TEM, as shown in Figure S2. All of the pyrolyzed Zn_xCo_y

https://doi.org/10.1021/jacs.3c11355
J. Am. Chem. Soc. XXXX, XXX, XXX−XXX

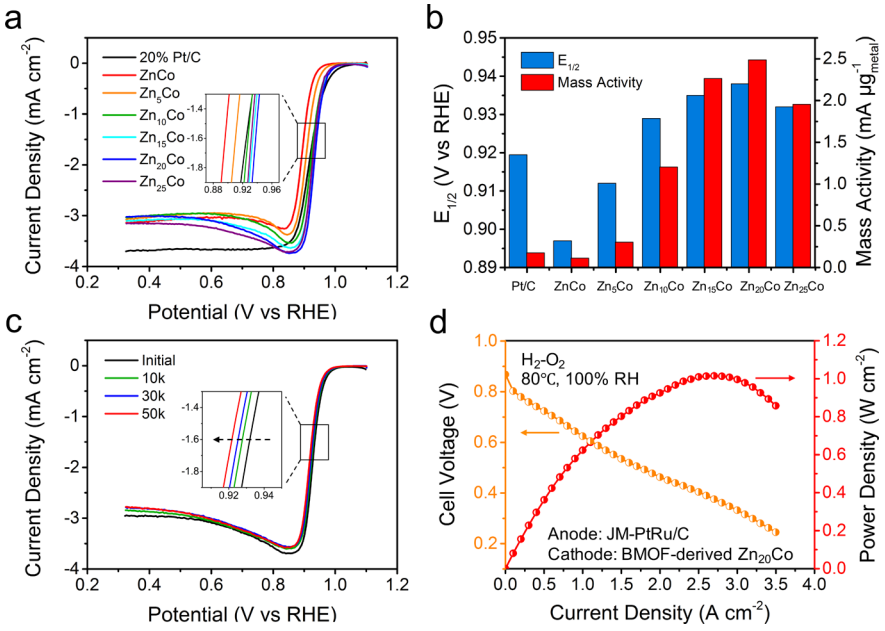

Figure 3. Electrochemical evaluation of BMOF-derived Zn_xCo_y as ORR catalysts in alkaline media. (a) ORR polarization curves of BMOF-derived Zn_xCo_y in O_2-saturated 1.0 M KOH at a scan rate of 5 mV/s and a rotation rate of 1600 rpm. Zn_xCo_y catalyst loading: 8 μg_{Co} cm^{-2}. 20% Pt/C loading: 25.5 μg_{Pt} cm^{-2}. Inset is the magnified $E_{1/2}$ region. (b) Comparison of the mass activity (MA) at 0.915 V vs RHE and half-wave potentials ($E_{1/2}$). (c) ORR polarization curves of BMOF-derived $Zn_{20}Co$ in O_2-saturated 1 M KOH at 1600 rpm and 5 mV/s after 10k, 30k, and 50k potential cycles from 0.6 to 1 V at 100 mV/s. Inset is the magnified $E_{1/2}$ region. (d) AEMFC tests with H_2 and O_2 at 80 °C and 100%RH. Anode catalyst: 60 wt % Pt−Ru/C (Johnson Matthey, 0.4 mg_{PtRu} cm^{-2}). Cathode catalyst: BMOF-derived $Zn_{20}Co$ (0.5 mg cm^{-2}).

materials maintained the polyhedral morphology of the BMOF precursors after heat treatment. There were evident metal nanoparticles distributed on the carbon substrate for pyrolyzed ZnCo and Zn_5Co, and a few small nanoparticles were observed in pyrolyzed $Zn_{10}Co$. In contrast, no metal nanoparticles were detected in the pyrolyzed $Zn_{15}Co$, $Zn_{20}Co$, and $Zn_{25}Co$ samples, which are consistent with the XRD results. The atomic-scale microstructures and chemical compositions of pyrolyzed $Zn_{20}Co$ were further investigated by aberration-corrected high-angle annular dark-field scanning transmission electron microscopy (HAADF-STEM) along with elemental EELS (Figure 1b−d). As observed in the EELS elemental mapping (Figure 1c), Co, Zn, and N elements were uniformly distributed throughout the MOF-derived structure. Since the HAADF image intensity is proportional to the atomic number ($I \propto Z^{1.7}$),[52] metal atoms are significantly brighter than the MOF-derived carbon support containing nonmetal C and N. Therefore, in Figure 1d, the bright spots marked by red circles with a size of about 3 Å correspond to atomically dispersed Co or Zn single atoms.

XPS measurements, shown in Figure S3a, validated the existence of Co, Zn, C, N and O elements in the pyrolyzed $Zn_{20}Co$. Accordingly, the high-resolution N 1s spectrum in Figure S3b could be deconvolved into four peaks: pyridinic N (398.4 eV, 64.17%), pyrrolic N (400.4 eV, 26.98%), graphitic N (402.4 eV, 6.38%), and N-oxide (404.3 eV, 2.47%) respectively. The Co 2p spectrum in Figure S3c exhibited two main peaks at 780.5 and 795.9 eV belonging to Co^{2+}, with two satellite peaks at 784.4 and 802.7 eV.[53−55] No metallic Co peak was found in the down-shifted region around 778.5 eV, further supporting the atomic dispersion of Co atoms.[56] As shown in Figure S3d, the Zn LMM auger peak was located at 988.3 eV, which indicated that the valence state of Zn was around +2. There was no signal that could be ascribed to metallic Zn.[57] It can be inferred that pyridinic N as the predominant configuration may enable coordination with Co or Zn atoms to generate Co−N_x or Zn−N_x structures, anchoring and stabilizing the atomically dispersed metal sites.[58,59]

XANES and EXAFS measurements were performed to investigate the electronic structure and coordination environment of Co and Zn atoms in $Zn_{20}Co$-BMOF-derived Zn/Co−N−C (pyrolyzed $Zn_{20}Co$). Figure 2a shows the normalized Co K-edge XANES spectra of Zn/Co−N−C, along with the data for Co foil, CoO, $Co(OH)_2$, Co_3O_4, and Co(II) phthalocyanine (CoPc) as references. Different from those of the references, the Zn/Co−N−C spectra presented relatively smooth XANES profiles. The pre-edge feature of Zn/Co−N−C at 7708 eV arises from the 1s to 3d transitions, and the low intensity is due to the centrosymmetric planar D_{4h} symmetry of Co−N_x structures.[44,56,60,61] The main edge absorption was assigned to the electronic transition from 1s to 4p orbitals and can be more precisely determined from the first derivative of XANES spectra as shown in Figure S4. The position of the absorption edge for Zn/Co−N−C at 7720 eV was near that for CoO and $Co(OH)_2$ (7721 eV) and lower than that for Co_3O_4, strongly suggesting a Co valence state of Co^{2+}, consistent with the XPS results. As presented in Figure 2c, the Fourier-transform (FT) for the k^3-weighted EXAFS profile (without phase correction) at the Co K-edge for Zn/Co−N−C only displayed one predominant peak at around 1.44 Å, corresponding to the Co−N scattering path in the first shell, which was slightly shorter than the Co−O path at 1.51 Å in Co_3O_4, 1.63 Å in $Co(OH)_2$ and 1.71 Å in CoO. Moreover, the absence of a Co−Co path at 2.18 Å and other high-order shell peaks in Zn/Co−N−C confirmed the atomically dispersed nature of Co sites, in good agreement with the atomic-scale HAADF-STEM observation (in Figure 1c). To

https://doi.org/10.1021/jacs.3c11355
J. Am. Chem. Soc. XXXX, XXX, XXX−XXX

more clearly distinguish the backscattering atoms, wavelet transform (WT) analysis of the Co K-edge EXAFS was carried out, which provided powerful resolution in both the radial distance and k space. As shown in Figures 2g and S5, the WT contour plots of Zn/Co−N−C presented only one intensity maximum at around 6 $Å^{-1}$, which was assigned to the Co−N scattering path. In contrast to the WT plots of Co foil, CoO, $Co(OH)_2$, and Co_3O_4, no intensity maximum related to Co−Co scattering path was observed at around 7−8 $Å^{-1}$ over the R range from 1 to 3 Å in Zn/Co−N−C. The coordination configuration and quantitative structural parameters of Co atoms in Zn/Co−N−C were further investigated by EXAFS fitting. The fitting profiles for the first shell are shown in Figure 2e in R space and Figure S6a in k space, and the corresponding fitting parameters are presented in Table S2. The best-fit analyses matched the experimental data well in both R and k space, following the Co−N scattering path. The fitted coordination number (CN) of Co atoms in the first shell was 3.99, and the mean bond length of Co−N was 1.91 Å. Based on the XANES and EXAFS analyses, the Co atoms in Zn/Co−N−C are atomically distributed in the MOF-derived N-doped porous carbon matrix, and one Co atom is coordinated by four N atoms to form the $Co-N_4$ structure, as shown in the inset of Figure 2e.

The normalized Zn K-edge XANES spectra of Zn/Co−N−C and Zn references, containing Zn foil, ZnO, and Zn(II) phthalocyanine (ZnPc), are presented in Figure 2b. There was no 1s−3d transition in the pre-edge region since Zn has full 3d orbitals. The absorption edge position of Zn/Co−N−C was located near that of ZnO, suggesting that the valence state of Zn was likely around +2 (Figure S4). As shown in Figure 2d, the k^3-weighted FT-EXAFS profile (without phase correction) at the Zn K-edge for Zn/Co−N−C exhibited a main peak at only around 1.51 Å, which is ascribed to the Zn−N scattering. The Zn−Zn path at 2.30 Å from Zn foil was negligible in Zn/Co−N−C, excluding the presence of metallic Zn and validating the atomic dispersion of Zn. Additionally, as shown in the WT-EXAFS contour plots of Zn/Co−N−C in Figure 2h, only one intensity maximum at 4.7 $Å^{-1}$ belonging to the Zn−N path was detected, and no intensity maximum related to the Zn−Zn contribution at 6.7 $Å^{-1}$ was observed. The first shell EXAFS fitting curves of Zn/Co−N−C using the Zn−N path in R space (Figure 2f) and k space (Figure S6b), respectively, were well-matched with the experimental data. As shown in Table S3, the fitted Zn−N first shell presents a CN of 4.14 at a distance of 2.02 Å, revealing the local atomic environment of Zn atoms, where one Zn atom is coordinated by four N atoms ($Zn-N_4$) and confined within the carbon matrix (inset of Figure 2f).

Electrocatalytic Performance. The electrochemical activities of the pyrolyzed Zn_xCo_y catalysts were evaluated in alkaline electrolyte via rotating-disk electrode (RDE) voltammetry. The ORR polarization curves were collected in an O_2-saturated 1.0 M KOH electrolyte solution at a scan rate of 5 mV/s and 1600 rpm, as shown in Figure 3a. It should be noted that the limiting current density is less than 4 mA cm^{-2}, rather than the commonly reported values in the range over 5−6 mA cm^{-2} in 0.1 M KOH, since the oxygen solubility in 1 M KOH is ∼70% of that in 0.1 M KOH.[62] The values of the half-wave potential ($E_{1/2}$) and mass activity (MA) at 0.915 V vs RHE are summarized in Figure 3b. The BMOF-derived $Zn_{15}Co$, $Zn_{20}Co$ and $Zn_{25}Co$ materials outperformed the other compositions of Zn_xCo_y due to their atomically dispersed metal sites without any large metal nanoparticles, according to XRD results (Figure S1b) and TEM images (Figure S2). Among them, the BMOF-derived $Zn_{20}Co$ exhibited the highest MA of 2.5 mA μg_{Co}^{-1} and $E_{1/2}$ of 0.938 V vs RHE, corresponding to a 12-fold increase in MA and a ∼20 mV positive shift in $E_{1/2}$, when compared to the benchmark Pt/C catalysts. It should be noted that the Co loading (8 μg_{Co} cm^{-2}) employed here is even lower than the Pt loading (25 μg_{Pt} cm^{-2}), suggesting the promising intrinsic electrocatalytic activity of atomically dispersed metal sites in BMOF-derived $Zn_{20}Co$.

The ORR selectivity of the BMOF-derived $Zn_{20}Co$ was assessed via the rotating ring-disk electrode technique, where a Pt ring was held at a constant potential (1.3 V vs RHE) to oxidize the H_2O_2 electrogenerated at the center disk electrode. As shown in Figure S8, over the potential region of 0.7−0.9 V where fuel cells generally operate, the H_2O_2 yield was below 10% and the electron transfer number was above 3.8, suggesting a near $4e^-$ transfer reaction.

The durability of the BMOF-derived $Zn_{20}Co$ was assessed in O_2-saturated 1 M KOH by scanning the potential at a rate of 100 mV/s over the potential range of 0.6−1 V versus RHE following an accelerated stress test protocol recommended by the U.S. Department of Energy. The cyclic voltammogram (CV) and ORR polarization profiles after 10k, 30k, and 50k cycles are compared with the initial ones in Figures S9 and 3c, respectively. The BMOF-derived $Zn_{20}Co$ exhibited a remarkable stability with an $E_{1/2}$ decay of only 3.2, 5.7, and 8.5 mV after 10k, 30k, and 50k cycles, respectively, compared to the initial one. The postdurability tested samples after 30k and 50k cycles were characterized by XAS. As shown in Figure S10, the positive shift in the normalized Co K-edge XANES indicated an increase in the valence state of Co after durability test. The corresponding k^3-weighted EXAFS in R space showed an evident increase of the first shell peak (at 1.45 Å) with a slight positive shift to 1.48 Å, indicating the addition of a Co−O scattering path in the first shell. In addition, there was an emergence and growth of a peak at around 2.5 Å, which was attributed to the Co−Co scattering path in cobalt oxide structures. Both XANES and EXAFS results suggested the possible oxidation of Co single atom sites to cobalt oxides after long-term durability testing in O_2-saturated electrolyte. Different from the Co sites, the Zn single atom sites remained stable without noticeable changes in either the XANES or EXAFS spectra, as shown in Figure S11. This suggests that Zn atoms may not actively participate in the ORR process as catalytic centers, which will be further clarified in the following *operando* XAS discussion.

The electrocatalytic effectiveness of BMOF-derived $Zn_{20}Co$ was further validated under realistic alkaline fuel cell working conditions via membrane electrode assembly (MEA) testing. The BMOF-derived $Zn_{20}Co$ was employed as the cathode catalyst, while a commercial 60 wt % PtRu/C was used as the anode catalyst in the H_2-O_2 fuel cell testing. As shown in Figure 3d, the BMOF-derived $Zn_{20}Co$ cathode with a catalyst loading of 0.5 mg cm^{-2} achieved an impressive PPD of 1.02 W cm^{-2} at 2.70 A cm^{-2}, representing the highest reported PPD among reported SACs in alkaline fuel cells.[45,49−51,63,64] The reported performance metrics of SACs in alkaline fuel cells are summarized in Table S4. More fuel cell testing results with different cathode loadings and durability analyses are shown in Figures S12 and S13, respectively. It should be noted that, even though the PPD of BMOF-derived $Zn_{20}Co$ is lower than that of a commercial 60% Pt/C (1.5 W cm^{-2} at the metal loading of

https://doi.org/10.1021/jacs.3c11355
J. Am. Chem. Soc. XXXX, XXX, XXX−XXX

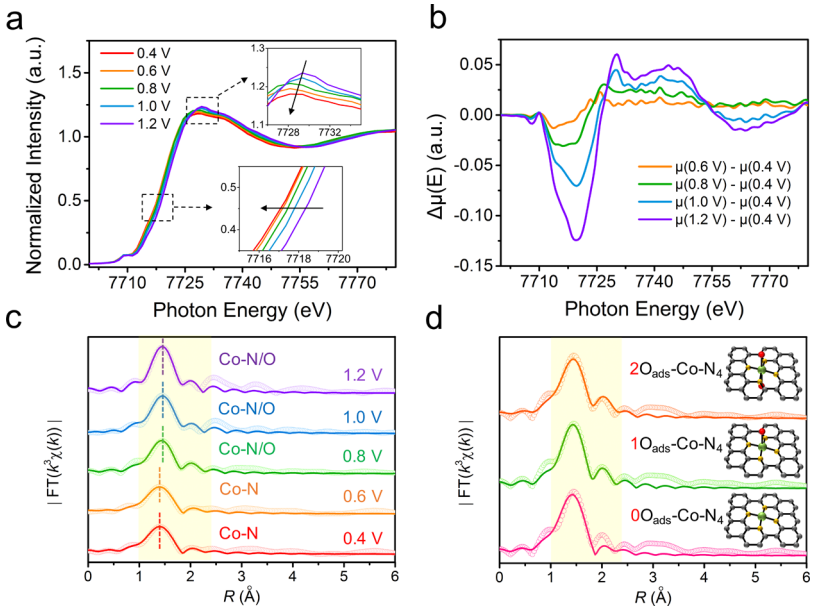

Figure 4. *Operando* XAS spectra of Co K-edge under electrochemical conditions. (a) *Operando* normalized Co K-edge XANES spectra of Zn_{20}Co-BMOF-derived Zn/Co−N−C under different applied potentials in O_2-saturated 1.0 M KOH. Insets show the magnified pre-edge and white-line regions. (b) Differential $\Delta\mu$ XANES spectra obtained by subtracting the normalized spectrum at every potential to the spectrum recorded at 0.4 V versus RHE. (c) Corresponding *operando* Co K-edge k^3-weighted FT-EXAFS fitting curves of Zn_{20}Co-BMOF-derived Zn/Co−N−C under different applied potentials at R space. The highlighted region in yellow was the fitting region. (d) Comparison of k^3-weighted FT-EXAFS fitting curves of Zn_{20}Co-BMOF-derived Zn/Co−N−C collected at 0.8 V versus RHE. Insets: schematic configuration model of Co centers with different numbers of O_{ads}. O(red), Co(green), N(yellow), and C(gray).

0.4 mg_{Pt} cm^{-2}) (Figure S14), the 0.5 mg cm^{-2} Zn_{20}Co cathode catalyst contained an ultralow Co metal loading of 0.8 μg_{Co} cm^{-2}, representing only 2% of the typical metal loading of 0.4 mg_{metal} cm^{-2} in fuel cells.[12,15,65] This points to the high intrinsic activity and efficiency of this nonprecious Zn/Co−N−C SAC and its potential for fuel cell applications.

***Operando* XAS of Zn/Co−N−C.** In an effort to unveil the nature of the electrocatalytic active sites in the Zn_{20}Co-BMOF-derived Zn/Co−N−C material under ORR conditions, *operando* XAS was performed to capture the dynamic changes of the electronic structure and local coordination environment for both Co and Zn centers. The cell design and experimental details can be found in the Supporting Information. The *operando* normalized Co K-edge XANES spectra are shown in Figure 4a, demonstrating a potential-dependent change in the oxidation state of Co. As shown in the magnified insets of the XANES spectra, when the applied potential was gradually decreased, there was a slight shift in the edge to lower photon energies, accompanied by a decrease in the white-line intensity. As shown in the first derivative of μ(E) (Figure S15), the absorption edge energy (E_0) was shifted negatively by ∼1.2 eV from 1.2 to 0.4 V vs RHE. This suggested that the oxidation state of Co decreased with more reducing potentials, as would be anticipated.

The differential $\Delta\mu$-XANES profile represents a spectral subtraction methodology that can be used to detect changes in single-atom sites, such as weakly bound adsorbate interactions.[66,67] In the Zn/Co−N−C material, the pristine Co single atom site should be adsorbate free (denoted as Co−N_4). However, the metal center will be oxidized to a higher valence state with an oxygen species adsorbed (denoted as O_{ads}−Co−N_4, where O_{ads} can be from different oxygen-related species, such as O_2, OH, OOH, ...) under higher applied potentials, causing a change in the XANES features. The $\Delta\mu$-XANES profile can be obtained by subtracting the XANES regions following the relationship:

$$\Delta\mu = \mu(O_{ads} - Co - N_4) - \mu(Co - N_4) \quad (1)$$

At 0.4 V vs RHE, the Co centers exist in a more reduced state when compared with higher applied potentials. Thus, the Co site at 0.4 V vs RHE was referred to the adsorbate-free state and its immediate coordination environment was Co−N_4. Consequently, the $\Delta\mu$-XANES signals in Figure 4b were generated according to the equation:

$$\Delta\mu = \mu(V) - \mu(0.4\ V) \quad (2)$$

The positive peak feature in the pre-edge region (∼7710 eV) indicated a coordination transition from a centrosymmetric environment (square planar Co−N_4) at 0.4 V to a non-centrosymmetric coordination geometry at higher applied potentials, likely due to the mild disruption by the presence of an axial oxygen atom via formation of O_{ads}−Co−N_4.[44,67] In addition, the shape of the $\Delta\mu$-XANES curves with the double peak maximum (at ∼7730 and ∼7745 eV) was consistent with prior reported theoretical results, supporting that the O_{ads} should be normal to the Co−N_4 plane; not in a planar mode.[68] Further, the intensity of the negative peak at ∼7720 eV increased with increasing applied potentials, which was related to the charge transfer from the Co atoms to the adsorbed oxygen species.

In addition to the *operando* XANES analysis, the *operando* EXAFS spectra can provide not only qualitative but also quantitative insights into the local coordination environment of the metal centers under the reaction conditions. The *operando* k^3-weighted FT-EXAFS spectra of the Co K-edge and the corresponding first-shell fitting curves are presented in Figure 4c. The fitting parameters are summarized in Table S5. When polarized to 0.4 and 0.6 V versus RHE, the dominant

https://doi.org/10.1021/jacs.3c11355
J. Am. Chem. Soc. XXXX, XXX, XXX−XXX

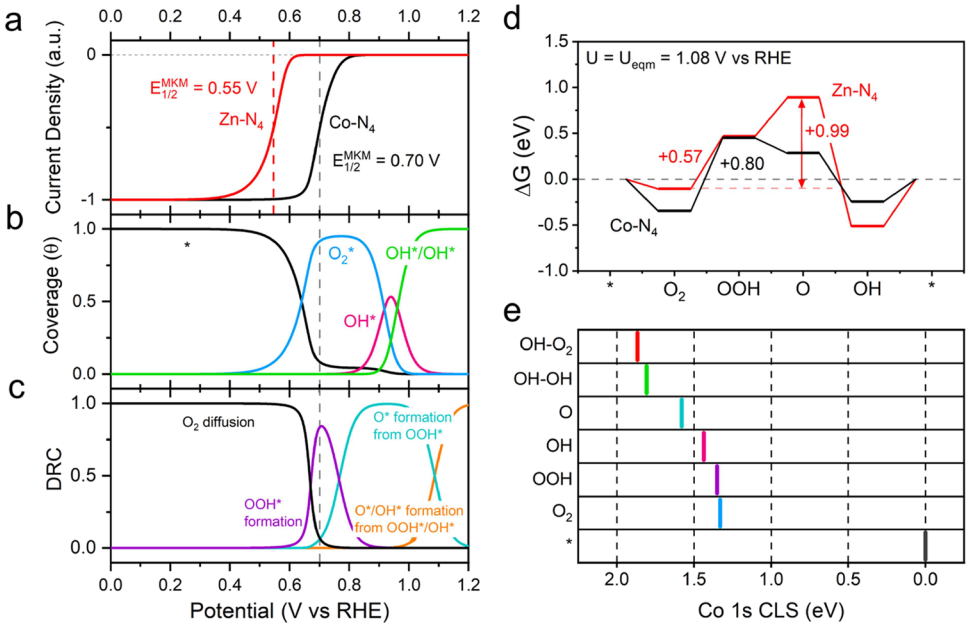

Figure 5. Potential-dependent microkinetic modeling predictions, showing (a) normalized electrochemical current density for Co−N_4 and Zn−N_4 sites, (b) coverage of Co−N_4 centers, and (c) degree of rate control (DRC) for Co−N_4. Gray and red vertical dashed lines in (a−c) denote the microkinetic modeling derived halfwave potential ($E_{1/2}^{MKM}$) for Co−N_4 and Zn−N_4, respectively. (d) Free energy diagram for the ORR over Co−N_4 and Zn−N_4 active sites at the DFT-derived equilibrium potential (U_{eqm}^{DFT}(PBE) = 1.08 V versus RHE). (e) Calculated Co 1s core level shifts (CLSs) as a response to adsorbed ORR intermediates with respect to the undecorated Co−N_4 site.

peak at 1.44 Å corresponds to a Co−N scattering path, with a CN of 4 and bond length of 1.91 Å. At higher applied potentials (0.8−1.2 V vs RHE), the peak shifts to a larger radial distance at around 1.47 Å with slightly enhanced amplitude, indicating the addition of a Co−O scattering path in the first shell. The fitting results showed a CN of ∼1 for the Co−O path, implying that one oxygen-related species (O_2 or OH from MKM predictions; vide infra) was adsorbed to the Co center in the Co−N_4 structure during the ORR process. After the adsorption of the oxygenated species, the CN of Co−N bonds was maintained at 4, while the bond length increased from 1.91 Å to 1.95−1.96 Å, representing a 2.1−2.6% elongation compared to the original undecorated state. Based on our electronic structure calculations, a similar increase in Co−N bond length was also observed upon the introduction of an adsorbed oxygen-containing species, resulting in a bond elongation ranging from 0.5 to 6.6% (Table S6). Such elongation of the Co−N bonds is due, at least in part, to distortion of the square planar Co−N_4 configuration by the oxygenated adsorbates, which is in accordance with the differential Δμ-XANES analysis. Moreover, to further investigate the local coordination environment of the O_{ads}-decorated Co center, the EXAFS data collected at 0.8 V versus RHE was fitted with different models by varying the number of O_{ads} from 0 to 2, as presented in Figure 4d and Table S7. For the 4-coordinate model without O_{ads}, the fitting curve was less well matched to the experimental data, and the dominant peak of the fitting curve shifted to lower R radius when compared with the experimental one. When a 6-coordinate configuration with 2 O_{ads} was applied, as illustrated in the inset of Figure 4d, the fitted CN of Co−N was 3.17. This indicated that one Co−N bond would be broken during the ORR process, destroying the stable Co−N_4 structure. In contrast, the 5-coordinate model including 1 oxygenated adsorbate gave rise to a much better fitting with more reasonable fitting parameters, supporting that only one oxygen species is adsorbed on the Co metal site to form the 1O_{ads}−Co−N_4 local structure during the ORR process. In summary, the *operando* XANES and EXAFS studies clearly indicate that the Co atom in square planar Co−N_4 is the ORR active center in the Zn/Co−N−C material, which can bind with one oxygen-containing adsorbate in the axial position and transfer charge to the adsorbed oxygen species.

The *operando* XAS spectra of the Zn K-edge are shown in Figure S16. In contrast to Co, the XANES spectra of the Zn K-edge exhibited no significant shift under different applied potentials, implying no evident valence change in the Zn atoms. In the Δμ-XANES profile (Figure S16c), there was no peak in the pre-edge region. The weak negative peak at 1.2 V versus RHE may be due to the slight degree of charge transfer from the center Zn atom to neighboring N atoms at high applied potentials. Moreover, the EXAFS spectra and fitting results (Figure S16d and Table S8) revealed that Zn−N_4 structures remained unchanged and no Zn−O coordination bonds were formed during the ORR process.

Electronic Structure Calculations. To provide additional insights into the nature of the active site in these Zn/Co−N−C materials, DFT calculations were performed to model the ORR over the Co−N_4 and Zn−N_4 sites. Within the computational hydrogen electrode formalism,[69] a lower ORR overpotential (η_{ORR}) was predicted for Zn−N_4 (η_{ORR} = 0.57 V) than Co−N_4 (η_{ORR} = 0.80 V), indicating the Zn−N_4 sites should be more active. However, this contradicted our experimental results (Figure S17). As previous works have shown, purely thermodynamic assessments are insufficient to accurately describe ORR activity trends for these Me−N_4 materials (Me: metal).[70,71] Accordingly, we constructed a potential-dependent MKM using our DFT-derived energetics to simulate current responses for Co−N_4 and Zn−N_4 active sites under the ORR conditions. Complete model details are

https://doi.org/10.1021/jacs.3c11355
J. Am. Chem. Soc. XXXX, XXX, XXX−XXX

included in the Supporting Information. As shown in Figure 5a, our MKM results revealed that Co−N_4 ($E_{1/2}$ = 0.70 V versus RHE) was much more active than Zn−N_4 ($E_{1/2}$ = 0.55 V vs RHE), in good agreement with the electrochemical experimental results. The corresponding potential-dependent coverage and degree of rate control (DRC) are shown in Figure 5b,c, respectively. The origin of this change in the relative activity between Co−N_4 and Zn−N_4 stems from the relative reaction energetics of sequential elementary steps. While purely thermochemical assessments of electrochemical activity rely on identifying the single elementary step with the least exergonic reaction energy, we find that this assessment is not appropriate for comparing relative activities between the Co−N_4 and Zn−N_4 sites. The source of the discrepancy between the conventional thermochemical assessment and microkinetic modeling results is most easily demonstrated by looking at the free energy diagrams for Co−N_4 and Zn−N_4 at the equilibrium potential (U_{eqm}^{DFT}(PBE) = 1.08 V vs RHE), as shown in Figure 5d. The protonation of O_2 to form the OOH* over Co−N_4 was the single most difficult elementary step (O_2* + (H^+ + e^-) → the OOH*; ΔG = +0.80 eV). However, over Zn−N_4, the presence of two sequential endergonic steps at elevated potentials relevant to the ORR resulted in a net energy barrier (O_2* + 2(H^+ + e^-) → O* + H_2O (aq); ΔG = +0.99 eV) higher than that of Co−N_4. These findings highlight the limitations of purely thermochemical assessments when evaluating electrochemical activity and illustrate how microkinetic modeling can be used to provide a more holistic assessment of electrocatalysts. Additionally, our MKM provides insight into the chemical decorations present on the Co metal center under ORR conditions. As shown in Figure 5b, the Co−N_4 metal center was undecorated at low potential, consistent with our *operando* EXAFS measurements. However, as the potential was increased toward active ORR conditions, we predicted the formation of Co−O bonds through either adsorbed O_2* or OH*. As indicated by DRC analysis (Figure 5c), the formation of OOH* from O_2* was the rate-limiting step over Co−N_4, leading to the accumulation of O_2* on the metal center. Similar microkinetic modeling results for Zn−N_4 are included in Figure S24.

To further distinguish the identity of the experimentally observed potential-dependent chemical decoration on the Co−N_4 center (and the apparent lack of chemical decoration on the Zn−N_4 center), we performed core level shift (CLS) calculations and Bader charge analysis on the chemically decorated systems. Calculations were performed on systems decorated by relevant ORR intermediates (Figures S18 and S21). Namely, we investigated the effect of adsorbed O_2, OOH, OH, and O species on both Co−N_4 and Zn−N_4, respectively. Additionally, we also considered coadsorbed states involving OH and O as these have been reported to facilitate the ORR over graphene-based SACs.[70,71] Thus, we interrogated the effects of the different adsorbates on the core−electron BE of the metal centers. Energetics for additional decorated states over Co−N_4 and Zn−N_4 are included in Table S9. The CLS calculation results showed that the effects of the adsorbates on the Co-ion and Zn-ion were dramatically different. For Co−N_4, all adsorbates induced a positive CLS. This positive shift indicated a shift toward higher binding energies with respect to the undecorated metal center. The calculated Co 1s CLSs were 1.33 (O_2), 1.35 (OOH), 1.44 (OH), and 1.58 eV (O) (Figure 5e). Coadsorbed states involving OH/OH (i.e., two adsorbed OH species) and OH/O_2 over Co−N_4, induced a shift to even higher binding energies of 1.81 and 1.86 eV, respectively, for the 1s core−electron state. Similar trends were observed for the Co 2p state for all adsorbates (Figure S19). The induced CLS for both Co 2p and Co 1s states correlated well ($R^2 \geq 0.89$) with the initial Bader charge on the decorated Co center for all adsorbates (Figure S20). The CLS correlation with the initial charge on the metal center indicated that the Co ion existed in slightly different oxidation states upon different decorations. This suggested that the shifts of the *operando* XANES spectra of the Co K-edge as a function of applied potential reported in Figure 4 were likely in part related to the existence of ORR intermediates adsorbed on the Co center. For the Zn−N_4 system, the CLS results were strikingly different as the binding energies shifted to lower energy values for most adsorbates with respect to the undecorated metal center. Notably, for adsorbed O on the Zn−N_4 site, the calculated shift was indistinguishable from the undecorated metal center. Detailed MKM and CLS analyses for Zn−N_4 sites are included in the Supporting Information (Figures S22−S25).

CONCLUSIONS

In summary, a class of Zn/Co−N−C SACs for alkaline ORR has been successfully prepared from Zn_xCo_y BMOF precursors. The single-atom states of both Co and Zn were thoroughly examined via STEM, EELS, XPS, and XAS, which revealed the square planar Co−N_4 and Zn−N_4 local configurations, respectively. The Zn_{20}Co-BMOF-derived Zn/Co−N−C displayed promising ORR performance not only in the RDE system but also under realistic alkaline fuel cell working conditions, reaching an impressive PPD of ∼1 W cm^{-2} at an ultralow Co loading of 8 μg_{Co} cm^{-2}. We conducted *operando* XAS to investigate the dynamic changes of both Co and Zn atoms during the ORR process to help reveal the underlying catalytic mechanism. The results suggested that the Co centers in the Co−N_4 structures worked as the primary active sites for the ORR, where one oxygenated species can be adsorbed in the axial direction to the Co−N_4 plane during the ORR process. The ORR activity of Co−N_4 and Zn−N_4 sites was further studied via a first-principles informed MKM, which validated that Co−N_4 metal centers served as the active sites for the ORR and Co−O bonds can be formed at elevated potentials (likely due to O_2* or OH* intermediates). To further elucidate the identity of the adsorbed oxygen species, Co 1s and 2p CLSs were calculated for the metal centers adsorbed with relevant ORR intermediates. The positive CLS shifts for Co upon adsorption by ORR intermediates suggested that the Co ion existed under slightly different oxidation states when decorated with various oxygenated adsorbates. Our findings provide constructive insights into the nature of the active site in the Zn/Co−N−C single-atom materials and their dynamic evolution under electrocatalytic conditions, which will help to pave the way for developing high-performance electrocatalysts for renewable energy applications.

ASSOCIATED CONTENT

Supporting Information

The Supporting Information is available free of charge at https://pubs.acs.org/doi/10.1021/jacs.3c11355.

Experimental details, additional XRD data, STEM images, CV curves, cyclic performance, XAS spectra, and details on electronic structure calculations (PDF)

https://doi.org/10.1021/jacs.3c11355
J. Am. Chem. Soc. XXXX, XXX, XXX−XXX

AUTHOR INFORMATION

Corresponding Authors

Manos Mavrikakis − *Department of Chemical & Biological Engineering, University of Wisconsin-Madison, Madison, Wisconsin 53706, United States;* orcid.org/0000-0002-5293-5356; Email: emavrikakis@wisc.edu

Héctor D. Abruña − *Department of Chemistry and Chemical Biology, Cornell University, Ithaca, New York 14853, United States;* orcid.org/0000-0002-3948-356X; Email: hda1@cornell.edu

Authors

Weixuan Xu − *Department of Chemistry and Chemical Biology, Cornell University, Ithaca, New York 14853, United States;* orcid.org/0000-0001-6171-4240

Rui Zeng − *Department of Chemistry and Chemical Biology, Cornell University, Ithaca, New York 14853, United States;* orcid.org/0000-0002-7577-767X

Michael Rebarchik − *Department of Chemical & Biological Engineering, University of Wisconsin-Madison, Madison, Wisconsin 53706, United States;* orcid.org/0000-0003-2008-825X

Alvaro Posada-Borbón − *Department of Chemical & Biological Engineering, University of Wisconsin-Madison, Madison, Wisconsin 53706, United States;* orcid.org/0000-0002-5245-099X

Huiqi Li − *Department of Chemistry and Chemical Biology, Cornell University, Ithaca, New York 14853, United States*

Christopher J. Pollock − *Cornell High Energy Synchrotron Source, Wilson Laboratory, Cornell University, Ithaca, New York 14853, United States;* orcid.org/0000-0001-5736-513X

Complete contact information is available at: https://pubs.acs.org/10.1021/jacs.3c11355

Author Contributions

‖W.X., R.Z., and M.R. contributed equally to this work.

Notes

The authors declare no competing financial interest.

ACKNOWLEDGMENTS

This work was supported by the Center for Alkaline Based Energy Solutions (CABES), part of the Energy Frontier Research Center (EFRC) program supported by the U.S. Department of Energy, under Grant DE-SC-0019445. This work made use of TEM facilities at the Cornell Center for Materials Research (CCMR) which are supported through the National Science Foundation Materials Research Science and Engineering Center (NSF MRSEC) program (DMR1719875). This work is based on research conducted at the Center for High-Energy X-ray Sciences (CHEXS), which is supported by the at National Science Foundation (BIO, ENG, and MPS Directorates) under award DMR-1829070. For the computational work, we used resources at the National Energy Research Scientific Computing Center, a DOE Office of Science User Facility that is supported by the DOE, Office of Science, under contract no. DE-AC02-05CH11231 using NERSC award BES-ERCAP0022773.

REFERENCES

(1) Debe, M. K. Electrocatalyst Approaches and Challenges for Automotive Fuel Cells. *Nature* **2012**, *486*, 43−51.

(2) Dunn, B.; Kamath, H.; Tarascon, J. M. Electrical Energy Storage for the Grid: A Battery of Choices. *Science* **2011**, *334*, 928−935.

(3) Chu, S.; Majumdar, A. Opportunities and Challenges for a Sustainable Energy Future. *Nature* **2012**, *488*, 294−303.

(4) Gasteiger, H. A.; Kocha, S. S.; Sompalli, B.; Wagner, F. T. Activity Benchmarks and Requirements for Pt, Pt-Alloy, and Non-Pt Oxygen Reduction Catalysts for PEMFCs. *Appl. Catal., B* **2005**, *56*, 9−35.

(5) Stamenkovic, V. R.; Strmcnik, D.; Lopes, P. P.; Markovic, N. M. Energy and Fuels from Electrochemical Interfaces. *Nat. Mater.* **2017**, *16*, 57−69.

(6) Yang, Y.; Xiong, Y.; Holtz, M. E.; Feng, X.; Zeng, R.; Chen, G.; DiSalvo, F. J.; Muller, D. A.; Abruña, H. D. Octahedral Spinel Electrocatalysts for Alkaline Fuel Cells. *Proc. Natl. Acad. Sci. U. S. A.* **2019**, *116*, 24425−24432.

(7) Lu, S.; Pan, J.; Huang, A.; Zhuang, L.; Lu, J. Alkaline Polymer Electrolyte Fuel Cells Completely Free from Noble Metal Catalysts. *Proc. Natl. Acad. Sci. U. S. A.* **2008**, *105*, 20611−20614.

(8) Yang, Y.; Peltier, C. R.; Zeng, R.; Schimmenti, R.; Li, Q.; Huang, X.; Yan, Z.; Potsi, G.; Selhorst, R.; Lu, X.; Xu, W.; Tader, M.; Soudackov, A. V.; Zhang, H.; Krumov, M.; Murray, E.; Xu, P.; Hitt, J.; Xu, L.; Ko, H. Y.; Ernst, B. G.; Bundschu, C.; Luo, A.; Markovich, D.; Hu, M.; He, C.; Wang, H.; Fang, J.; Distasio, R. A.; Kourkoutis, L. F.; Singer, A.; Noonan, K. J. T.; Xiao, L.; Zhuang, L.; Pivovar, B. S.; Zelenay, P.; Herrero, E.; Feliu, J. M.; Suntivich, J.; Giannelis, E. P.; Hammes-Schiffer, S.; Arias, T.; Mavrikakis, M.; Mallouk, T. E.; Brock, J. D.; Muller, D. A.; Disalvo, F. J.; Coates, G. W.; Abruña, H. D. Electrocatalysis in Alkaline Media and Alkaline Membrane-Based Energy Technologies. *Chem. Rev.* **2022**, *122*, 6117−6321.

(9) Retuerto, M.; Calle-Vallejo, F.; Pascual, L.; Lumbeeck, G.; María; Fernandez-Diaz, T.; Croft, M.; Gopalakrishnan, J.; Peñ, M. A.; Hadermann, J.; Greenblatt, M.; Rojas, S. $La_{1.5}Sr_{0.5}NiMn_{0.5}Ru_{0.5}O_6$ Double Perovskite with Enhanced ORR/OER Bifunctional Catalytic Activity. *ACS Appl. Mater. Interfaces* **2019**, *11*, 21454−21464.

(10) Seok, J.; Molina Villarino, A.; Shi, Z.; Yang, Y.; Ahmadi, M.; Muller, D. A.; Disalvo, F. J.; Abruñ, H. D. La-Based Perovskite Oxide Catalysts for Alkaline Oxygen Reduction: The Importance of Electrochemical Stability. *J. Phys. Chem. C* **2022**, *126*, 3098−3108.

(11) Suntivich, J.; Gasteiger, H. A.; Yabuuchi, N.; Nakanishi, H.; Goodenough, J. B.; Shao-Horn, Y. Design Principles for Oxygen-Reduction Activity on Perovskite Oxide Catalysts for Fuel Cells and Metal-Air Batteries. *Nat. Chem.* **2011**, *3*, 546−550.

(12) Wang, Y.; Yang, Y.; Jia, S.; Wang, X.; Lyu, K.; Peng, Y.; Zheng, H.; Wei, X.; Ren, H.; Xiao, L.; Wang, J.; Muller, D. A.; Abruña, H. D.; Hwang, B. J.; Lu, J.; Zhuang, L. Synergistic Mn-Co Catalyst Outperforms Pt on High-Rate Oxygen Reduction for Alkaline Polymer Electrolyte Fuel Cells. *Nat. Commun.* **2019**, *10*, 1506.

(13) Zhao, Q.; Yan, Z.; Chen, C.; Chen, J. Spinels: Controlled Preparation, Oxygen Reduction/Evolution Reaction Application, and Beyond. *Chem. Rev.* **2017**, *117*, 10121−10211.

(14) Yang, Y.; Wang, Y.; Xiong, Y.; Huang, X.; Shen, L.; Huang, R.; Wang, H.; Pastore, J. P.; Yu, S. H.; Xiao, L.; Brock, J. D.; Zhuang, L.; Abruña, H. D. *In Situ* X-Ray Absorption Spectroscopy of a Synergistic Co-Mn Oxide Catalyst for the Oxygen Reduction Reaction. *J. Am. Chem. Soc.* **2019**, *141*, 1463−1466.

(15) Zeng, R.; Yang, Y.; Feng, X.; Li, H.; Gibbs, L. M.; DiSalvo, F. J.; Abruña, H. D. Nonprecious Transition Metal Nitrides as Efficient Oxygen Reduction Electrocatalysts for Alkaline Fuel Cells. *Sci. Adv.* **2022**, *8*, 1584.

(16) Wu, H.; Chen, W. Copper Nitride Nanocubes: Size-Controlled Synthesis and Application as Cathode Catalyst in Alkaline Fuel Cells. *J. Am. Chem. Soc.* **2011**, *133*, 15236−15239.

(17) Yuan, Y.; Wang, J.; Adimi, S.; Shen, H.; Thomas, T.; Ma, R.; Attfield, J. P.; Yang, M. Zirconium Nitride Catalysts Surpass Platinum for Oxygen Reduction. *Nat. Mater.* **2020**, *19*, 282−286.

(18) Lin, L.; Zhu, Q.; Xu, A. W. Noble-Metal-Free Fe-N/C Catalyst for Highly Efficient Oxygen Reduction Reaction under Both Alkaline and Acidic Conditions. *J. Am. Chem. Soc.* **2014**, *136*, 11027−11033.

(19) Yang, J.; Liu, W.; Xu, M.; Liu, X.; Qi, H.; Zhang, L.; Yang, X.; Niu, S.; Zhou, D.; Liu, Y.; Su, Y.; Li, J. F.; Tian, Z. Q.; Zhou, W.; Wang, A.; Zhang, T. Dynamic Behavior of Single-Atom Catalysts in Electrocatalysis: Identification of Cu-N_3 as an Active Site for the Oxygen Reduction Reaction. *J. Am. Chem. Soc.* **2021**, *143*, 14530−14539.
(20) Bates, J. S.; Biswas, S.; Suh, S. E.; Johnson, M. R.; Mondal, B.; Root, T. W.; Stahl, S. S. Chemical and Electrochemical O_2 Reduction on Earth-Abundant M-N-C Catalysts and Implications for Mediated Electrolysis. *J. Am. Chem. Soc.* **2022**, *144*, 922−927.
(21) Cao, L.; Luo, Q.; Liu, W.; Lin, Y.; Liu, X.; Cao, Y.; Zhang, W.; Wu, Y.; Yang, J.; Yao, T.; Wei, S. Identification of Single-Atom Active Sites in Carbon-Based Cobalt Catalysts during Electrocatalytic Hydrogen Evolution. *Nat. Catal.* **2019**, *2*, 134−141.
(22) Gu, J.; Hsu, C. S.; Bai, L.; Chen, H. M.; Hu, X. Atomically Dispersed Fe^{3+} Sites Catalyze Efficient CO_2 Electroreduction to CO. *Science* **2019**, *364*, 1091−1094.
(23) Shang, H.; Zhou, X.; Dong, J.; Li, A.; Zhao, X.; Liu, Q.; Lin, Y.; Pei, J.; Li, Z.; Jiang, Z.; Zhou, D.; Zheng, L.; Wang, Y.; Zhou, J.; Yang, Z.; Cao, R.; Sarangi, R.; Sun, T.; Yang, X.; Zheng, X.; Yan, W.; Zhuang, Z.; Li, J.; Chen, W.; Wang, D.; Zhang, J.; Li, Y. Engineering Unsymmetrically Coordinated Cu-S_1N_3 Single Atom Sites with Enhanced Oxygen Reduction Activity. *Nat. Commun.* **2020**, *11*, 3049.
(24) Sun, T.; Zhao, S.; Chen, W.; Zhai, D.; Dong, J.; Wang, Y.; Zhang, S.; Han, A.; Gu, L.; Yu, R.; Wen, X.; Ren, H.; Xu, L.; Chen, C.; Peng, Q.; Wang, D.; Li, Y. Single-Atomic Cobalt Sites Embedded in Hierarchically Ordered Porous Nitrogen-Doped Carbon as a Superior Bifunctional Electrocatalyst. *Proc. Natl. Acad. Sci. U. S. A.* **2018**, *115*, 12692−12697.
(25) Li, Z.; Ji, S.; Liu, Y.; Cao, X.; Tian, S.; Chen, Y.; Niu, Z.; Li, Y. Well-Defined Materials for Heterogeneous Catalysis: From Nanoparticles to Isolated Single-Atom Sites. *Chem. Rev.* **2020**, *120*, 623−682.
(26) Lu, B.; Liu, Q.; Chen, S. Electrocatalysis of Single-Atom Sites: Impacts of Atomic Coordination. *ACS Catal.* **2020**, *10*, 7584−7618.
(27) Liu, L.; Corma, A. Metal Catalysts for Heterogeneous Catalysis: From Single Atoms to Nanoclusters and Nanoparticles. *Chem. Rev.* **2018**, *118*, 4981−5079.
(28) Han, A.; Wang, B.; Kumar, A.; Qin, Y.; Jin, J.; Wang, X.; Yang, C.; Dong, B.; Jia, Y.; Liu, J.; Sun, X.; Han, A.; Wang, B.; Kumar, A.; Qin, Y.; Jin, J.; Wang, X.; Yang, C.; Dong, B.; Jia, Y.; Liu, J.; Sun, X. Recent Advances for MOF-Derived Carbon-Supported Single-Atom Catalysts. *Small Methods* **2019**, *3*, No. 1800471.
(29) Shang, L.; Yu, H.; Huang, X.; Bian, T.; Shi, R.; Zhao, Y.; Waterhouse, G. I. N.; Wu, L.-Z.; Tung, C.-H.; Zhang, T.; Shang, L.; Yu, H.; Huang, X.; Bian, T.; Zhao, Y. F.; Wu, L.-Z.; Tung, C.-H.; Zhang, T.; Shi, M. R.; Waterhouse, G. I. N. Well-Dispersed ZIF-Derived Co,N-Co-Doped Carbon Nanoframes through Mesoporous-Silica-Protected Calcination as Efficient Oxygen Reduction Electrocatalysts. *Adv. Mater.* **2016**, *28*, 1668−1674.
(30) Song, Z.; Zhang, L.; Doyle-Davis, K.; Fu, X.; Luo, J. L.; Sun, X. Recent Advances in MOF-Derived Single Atom Catalysts for Electrochemical Applications. *Adv. Energy Mater.* **2020**, *10*, No. 2001561.
(31) Xie, X.; Peng, L.; Yang, H.; Waterhouse, G. I. N; Shang, L.; Zhang, T.; Xie, X.; Yang, H.; Shang, L.; Zhang, T.; Peng, L.; Waterhouse, G. I. N MIL-101-Derived Mesoporous Carbon Supporting Highly Exposed Fe Single-Atom Sites as Efficient Oxygen Reduction Reaction Catalysts. *Adv. Mater.* **2021**, *33*, No. 2101038.
(32) Chen, Y.-Z.; Wang, C.; Wu, Z.-Y.; Xiong, Y.; Xu, Q.; Yu, S.-H.; Jiang, H.-L.; Chen, Y.; Wang, C.; Wu, Z.; Xiong, Y.; Yu, S.; Jiang, H.; Xu, Q. From Bimetallic Metal-Organic Framework to Porous Carbon: High Surface Area and Multicomponent Active Dopants for Excellent Electrocatalysis. *Adv. Mater.* **2015**, *27*, 5010−5016.
(33) Xiong, Y.; Yang, Y.; DiSalvo, F. J.; Abruña, H. D. Synergistic Bimetallic Metallic Organic Framework-Derived Pt-Co Oxygen Reduction Electrocatalysts. *ACS Nano* **2020**, *14*, 13069−13080.
(34) Xu, W.; Yoon, D.; Yang, Y.; Xiong, Y.; Li, H.; Zeng, R.; Muller, D. A.; Abruña, H. D. MOF-Derived Bimetallic Pd-Co Alkaline ORR Electrocatalysts. *ACS Appl. Mater. Interfaces* **2022**, *14*, 44735−44744.
(35) Kropp, T.; Mavrikakis, M. Transition Metal Atoms Embedded in Graphene: How Nitrogen Doping Increases CO Oxidation Activity. *ACS Catal.* **2019**, *9*, 6864−6868.
(36) Chen, S.; Cui, M.; Yin, Z.; Xiong, J.; Mi, L.; Li, Y. Single-Atom and Dual-Atom Electrocatalysts Derived from Metal Organic Frameworks: Current Progress and Perspectives. *ChemSusChem* **2021**, *14*, 73−93.
(37) Tong, M.; Sun, F.; Xie, Y.; Wang, Y.; Yang, Y.; Tian, C.; Wang, L.; Fu, H. Operando Cooperated Catalytic Mechanism of Atomically Dispersed Cu−N_4 and Zn−N_4 for Promoting Oxygen Reduction Reaction. *Angew. Chem., Int. Ed.* **2021**, *60*, 14005−14012.
(38) Meng, Z.; Cai, S.; Wang, R.; Tang, H.; Song, S.; Tsiakaras, P. Bimetallic−organic Framework-Derived Hierarchically Porous Co-Zn-N-C as Efficient Catalyst for Acidic Oxygen Reduction Reaction. *Appl. Catal., B* **2019**, *244*, 120−127.
(39) Menga, D.; Low, J. L.; Li, Y. S.; Arčon, I.; Koyutürk, B.; Wagner, F.; Ruiz-Zepeda, F.; Gaberšček, M.; Paulus, B.; Fellinger, T. P. Resolving the Dilemma of Fe-N-C Catalysts by the Selective Synthesis of Tetrapyrrolic Active Sites via an Imprinting Strategy. *J. Am. Chem. Soc.* **2021**, *143*, 18010−18019.
(40) Menga, D.; Ruiz-Zepeda, F.; Moriau, L.; Šala, M.; Wagner, F.; Koyutürk, B.; Bele, M.; Petek, U.; Hodnik, N.; Gaberšček, M.; Fellinger, T. P. Active-Site Imprinting: Preparation of Fe−N−C Catalysts from Zinc Ion−Templated Ionothermal Nitrogen-Doped Carbons. *Adv. Energy Mater.* **2019**, *9*, No. 1902412.
(41) Li, Y.; Yang, F.; Gai, P. L.; Boyes, E. D. *In-Situ* Environmental (Scanning) Transmission Electron Microscopy of Catalysts at the Atomic Level. *J. Phys. Conf. Ser.* **2014**, *522*, No. 012002.
(42) Liu, L.; Zakharov, D. N.; Arenal, R.; Concepcion, P.; Stach, E. A.; Corma, A. Evolution and Stabilization of Subnanometric Metal Species in Confined Space by in Situ TEM. *Nat. Commun.* **2018**, *9*, 574.
(43) Li, X.; Yang, X.; Zhang, J.; Huang, Y.; Liu, B. In Situ/Operando Techniques for Characterization of Single-Atom Catalysts. *ACS Catal.* **2019**, *9*, 2521−2531.
(44) Lien, H. T.; Chang, S. T.; Chen, P. T.; Wong, D. P.; Chang, Y. C.; Lu, Y. R.; Dong, C. L.; Wang, C. H.; Chen, K. H.; Chen, L. C. Probing the Active Site in Single-Atom Oxygen Reduction Catalysts via Operando X-Ray and Electrochemical Spectroscopy. *Nat. Commun.* **2020**, *11*, 4233.
(45) Xing, G.; Tong, M.; Yu, P.; Wang, L.; Zhang, G.; Tian, C.; Fu, H. Reconstruction of Highly Dense Cu−N_4 Active Sites in Electrocatalytic Oxygen Reduction Characterized by Operando Synchrotron Radiation. *Angew. Chem., Int. Ed.* **2022**, *61*, No. e202211098.
(46) Li, J.; Banis, M. N.; Ren, Z.; Adair, K. R.; Doyle-Davis, K.; Meira, D. M.; Finfrock, Y. Z.; Zhang, L.; Kong, F.; Sham, T. K.; Li, R.; Luo, J.; Sun, X. Unveiling the Nature of Pt Single-Atom Catalyst during Electrocatalytic Hydrogen Evolution and Oxygen Reduction Reactions. *Small* **2021**, *17*, No. 2007245.
(47) Zitolo, A.; Ranjbar-Sahraie, N.; Mineva, T.; Li, J.; Jia, Q.; Stamatin, S.; Harrington, G. F.; Lyth, S. M.; Krtil, P.; Mukerjee, S.; Fonda, E.; Jaouen, F. Identification of Catalytic Sites in Cobalt-Nitrogen-Carbon Materials for the Oxygen Reduction Reaction. *Nat. Commun.* **2017**, *8*, 957.
(48) Han, G.; Zhang, X.; Liu, W.; Zhang, Q.; Wang, Z.; Cheng, J.; Yao, T.; Gu, L.; Du, C.; Gao, Y.; Yin, G. Substrate Strain Tunes Operando Geometric Distortion and Oxygen Reduction Activity of CuN_2C_2 Single-Atom Sites. *Nat. Commun.* **2021**, *12*, 6335.
(49) Li, J. C.; Maurya, S.; Kim, Y. S.; Li, T.; Wang, L.; Shi, Q.; Liu, D.; Feng, S.; Lin, Y.; Shao, M. Stabilizing Single-Atom Iron Electrocatalysts for Oxygen Reduction via Ceria Confining and Trapping. *ACS Catal.* **2020**, *10*, 2452−2458.
(50) Cui, L.; Cui, L.; Li, Z.; Zhang, J.; Wang, H.; Lu, S.; Xiang, Y. A Copper Single-Atom Catalyst towards Efficient and Durable Oxygen Reduction for Fuel Cells. *J. Mater. Chem. A* **2019**, *7*, 16690−16695.

https://doi.org/10.1021/jacs.3c11355
J. Am. Chem. Soc. XXXX, XXX, XXX−XXX

(51) Zhao, Y. M.; Zhang, P. C.; Xu, C.; Zhou, X. Y.; Liao, L. M.; Wei, P. J.; Liu, E.; Chen, H.; He, Q.; Liu, J. G. Design and Preparation of Fe-N5 Catalytic Sites in Single-Atom Catalysts for Enhancing the Oxygen Reduction Reaction in Fuel Cells. *ACS Appl. Mater. Interfaces* **2020**, *12*, 17334−17342.
(52) Kirkland, E. J.; Loane, R. F.; Silcox, J. Simulation of Annular Dark Field Stem Images Using a Modified Multislice Method. *Ultramicroscopy* **1987**, *23*, 77−96.
(53) Biesinger, M. C.; Payne, B. P.; Grosvenor, A. P.; Lau, L. W. M.; Gerson, A. R.; Smart, R. S. C. Resolving Surface Chemical States in XPS Analysis of First Row Transition Metals, Oxides and Hydroxides: Cr, Mn, Fe. *Co and Ni. Appl. Surf. Sci.* **2011**, *257*, 2717−2730.
(54) Zhang, M.; Dai, Q.; Zheng, H.; Chen, M.; Dai, L. Novel MOF-Derived Co@N-C Bifunctional Catalysts for Highly Efficient Zn−Air Batteries and Water Splitting. *Adv. Mater.* **2018**, *30*, No. 1705431.
(55) Sun, Y.; Silvioli, L.; Sahraie, N. R.; Ju, W.; Li, J.; Zitolo, A.; Li, S.; Bagger, A.; Arnarson, L.; Wang, X.; Moeller, T.; Bernsmeier, D.; Rossmeisl, J.; Frédé, F.; Jaouen, F.; Strasser, P. Activity−Selectivity Trends in the Electrochemical Production of Hydrogen Peroxide over Single-Site Metal−Nitrogen−Carbon Catalysts. *J. Am. Chem. Soc.* **2019**, *141*, 12372−12381.
(56) Wang, P.; Ren, Y.; Wang, R.; Zhang, P.; Ding, M.; Li, C.; Zhao, D.; Qian, Z.; Zhang, Z.; Zhang, L.; Yin, L. Atomically Dispersed Cobalt Catalyst Anchored on Nitrogen-Doped Carbon Nanosheets for Lithium-Oxygen Batteries. *Nat. Commun.* **2020**, *11*, 1576.
(57) Deroubaix, G.; Marcus, P. X-ray Photoelectron Spectroscopy Analysis of Copper and Zinc Oxides and Sulphides. *Surf. Interface Anal.* **1992**, *18*, 39−46.
(58) Zhang, L.; Shang, N.; Gao, S.; Wang, J.; Meng, T.; Du, C.; Shen, T.; Huang, J.; Wu, Q.; Wang, H.; Qiao, Y.; Wang, C.; Gao, Y.; Wang, Z. Atomically Dispersed Co Catalyst for Efficient Hydrodeoxygenation of Lignin-Derived Species and Hydrogenation of Nitroaromatics. *ACS Catal.* **2020**, *10*, 8672−8682.
(59) Zang, W.; Sumboja, A.; Ma, Y.; Zhang, H.; Wu, Y.; Wu, S.; Wu, H.; Liu, Z.; Guan, C.; Wang, J.; Pennycook, S. J. Single Co Atoms Anchored in Porous N-Doped Carbon for Efficient Zinc-Air Battery Cathodes. *ACS Catal.* **2018**, *8*, 8961−8969.
(60) Wan, W.; Triana, C. A.; Lan, J.; Li, J.; Allen, C. S.; Zhao, Y.; Iannuzzi, M.; Patzke, G. R. Bifunctional Single Atom Electrocatalysts: Coordination−performance Correlations and Reaction Pathways. *ACS Nano* **2020**, *14*, 13279−13293.
(61) Zhu, Y.; Sun, W.; Luo, J.; Chen, W.; Cao, T.; Zheng, L.; Dong, J.; Zhang, J.; Zhang, M.; Han, Y.; Chen, C.; Peng, Q.; Wang, D.; Li, Y. A Cocoon Silk Chemistry Strategy to Ultrathin N-Doped Carbon Nanosheet with Metal Single-Site Catalysts. *Nat. Commun.* **2018**, *9*, 3861.
(62) Davis, R. E.; Horvath, G. L.; Tobias, C. W. The Solubility and Diffusion Coefficient of Oxygen in Potassium Hydroxide Solutions. *Electrochim. Acta* **1967**, *12*, 287−297.
(63) Shah, S. S. A.; Najam, T.; Bashir, M. S.; Peng, L.; Nazir, M. A.; Javed, M. S. Single-Atom Catalysts for next-Generation Rechargeable Batteries and Fuel Cells. *Energy Storage Mater.* **2022**, *45*, 301−322.
(64) Ferrero, G. A.; Preuss, K.; Marinovic, A.; Jorge, A. B.; Mansor, N.; Brett, D. J. L.; Fuertes, A. B.; Sevilla, M.; Titirici, M.-M. Fe−N-Doped Carbon Capsules with Outstanding Electrochemical Performance and Stability for the Oxygen Reduction Reaction in Both Acid and Alkaline Conditions. *ACS Nano* **2016**, *10*, 5922−5932.
(65) Yang, Y.; Peng, H.; Xiong, Y.; Li, Q.; Lu, J.; Xiao, L.; Disalvo, F. J.; Zhuang, L.; Abrunã, H. D. High-Loading Composition-Tolerant Co-Mn Spinel Oxides with Performance beyond 1 W/cm^2 in Alkaline Polymer Electrolyte Fuel Cells. *ACS Energy Lett.* **2019**, *4*, 1251−1257.
(66) van Bokhoven, J. Recent Developments in X-Ray Absorption Spectroscopy. *Phys. Chem. Chem. Phys.* **2010**, *12*, 5502−5502.
(67) Ramaswamy, N.; Mukerjee, S. Fundamental Mechanistic Understanding of Electrocatalysis of Oxygen Reduction on Pt and Non-Pt Surfaces: Acid versus Alkaline Media. *Adv. Phys. Chem.* **2012**, *2012*, No. 491604.
(68) Ziegelbauer, J. M.; Olson, T. S.; Pylypenko, S.; Alamgir, F.; Jaye, C.; Atanassov, P.; Mukerjee, S. Direct Spectroscopic Observation of the Structural Origin of Peroxide Generation from Co-Based Pyrolyzed Porphyrins for ORR Applications. *J. Phys. Chem. C* **2008**, *112*, 8839−8849.
(69) Nørskov, J. K.; Rossmeisl, J.; Logadottir, A.; Lindqvist, L.; Kitchin, J. R.; Bligaard, T.; Jónsson, H. Origin of the Overpotential for Oxygen Reduction at a Fuel-Cell Cathode. *J. Phys. Chem. B* **2004**, *108*, 17886−17892.
(70) Rebarchik, M.; Bhandari, S.; Kropp, T.; Mavrikakis, M. How Noninnocent Spectator Species Improve the Oxygen Reduction Activity of Single-Atom Catalysts: Microkinetic Models from First-Principles Calculations. *ACS Catal.* **2020**, *10*, 9129−9135.
(71) Wang, Y.; Tang, Y. J.; Zhou, K. Self-Adjusting Activity Induced by Intrinsic Reaction Intermediate in Fe-N-C Single-Atom Catalysts. *J. Am. Chem. Soc.* **2019**, *141*, 14115−14119.

https://doi.org/10.1021/jacs.3c11355
J. Am. Chem. Soc. XXXX, XXX, XXX−XXX